Multiband nature of room-temperature superconductivity in LaH_{10} at high pressure

Chongze Wang, Seho Yi, and Jun-Hyung Cho*

Department of Physics, Research Institute for Natural Science, and HYU-HPSTAR-CIS High Pressure Research Center, Hanyang University, 222 Wangsimni-ro, Seongdong-Ku, Seoul 04763, Republic of Korea

(Received 28 September 2019; revised manuscript received 24 February 2020; accepted 27 February 2020; published 13 March 2020)

Recently, the discovery of room-temperature superconductivity (SC) was experimentally realized in the fcc phase of LaH_{10} under megabar pressures. This SC of compressed LaH_{10} has been explained in terms of strong electron-phonon coupling (EPC), but the detailed nature of how the large EPC constant and high superconducting transition temperature T_c are attained has not yet been clearly identified. Based on the density-functional theory and the Migdal-Eliashberg formalism, we reveal the presence of two nodeless, anisotropic superconducting gaps on the Fermi surface (FS). Here, the small gap is mostly associated with the hybridized states of H s and La f orbitals on the three outer FS sheets, while the large gap arises mainly from the hybridized state of neighboring H s or p orbitals on the one inner FS sheet. Further, we find that compressed YH_{10} with the same sodalitelike clathrate structure has the two additional FS sheets, enhancing EPC constant and T_c. It is thus demonstrated that the nature of room-temperature SC in compressed LaH_{10} and YH_{10} features the multiband pairing of hybridized electronic states with large EPC constants.

DOI: 10.1103/PhysRevB.101.104506

The realization of superconductivity (SC) at room temperature is one of the most challenging subjects in modern physics and chemistry. Recently, two experimental groups synthesized the lanthanum hydride LaH_{10} with a sodalitelike clathrate structure [see Fig. 1(a)] at megabar pressures and measured a superconducting transition temperature T_c of 250–260 K at a pressure of ∼170 GPa [1,2]. Obviously, this record of T_c is the highest among so far experimentally available superconducting materials [3–6], thereby opening a new era of high-T_c SC [7,8].

Historically, a search for room-temperature SC in compressed hydrides dates back to about half a century ago. Based on the Bardeen-Cooper-Schrieffer (BCS) theory [9], Neil Ashcroft [10] proposed a pioneering idea that the metallization of hydrogen under high pressures over ∼400 GPa could exhibit a high-T_c SC [11–13]. Since then, in order to achieve metallic hydrogen at relatively lower pressures attainable using diamond anvil cells [14,15], many binary hydrides have been theoretically searched [7,8,16–22], among which rare-earth hydrides such as the fcc phases of YH_{10} and LaH_{10} exhibited room-temperature SC at around 200–300 GPa [21,22]. Recently, a number of density functional theory (DFT) studies [21–26] have been intensively performed to show that fcc LaH_{10} having a high crystalline symmetry of the space group $Fm\bar{3}m$ (No. 225) with the point group O_h features the peculiar bonding characters with anionic La, anionic H_1 [forming the squares in Fig. 1(a)], and cationic H_2 [forming the hexagons in Fig. 1(a)] atoms, van Hove singularities near the Fermi energy E_f, and strong electron-phonon coupling (EPC) with H-derived phonon modes. These unique bonding, electronic, and phononic properties of fcc LaH_{10} have been associated with increased EPC constant, leading to the emergence of a room-temperature SC. However, the detailed nature of how fcc LaH_{10} forms the large EPC constant and high T_c remains to be clarified.

In this paper, using the DFT calculations [27] and the Migdal-Eliashberg formalism [28–30], we explore the nature of the superconducting gap in fcc LaH_{10}. Our analysis of the momentum-resolved superconducting gap reveals that there are two nodeless, anisotropic superconducting gaps on the Fermi surface (FS), representing a two-gap SC with s-wave symmetry. It is found that at 20 K, the small gap in the range of 41–52 meV is mostly associated with the hybridized states of H_1 s and La f orbitals on the three outer FS sheets, while the large gap in the range of 60–66 meV arises mainly from the hybridized state of H_1 s or p and H_2 s orbitals on the one inner FS sheet. Interestingly, for fcc YH_{10} having the same sodalitelike clathrate structure, we find that the four FS sheets whose patterns are similar to those of fcc LaH_{10} slightly shift upward because the two additional FS sheets arising from Y d orbitals are occupied. The resulting six FS sheets of fcc YH_{10} not only contribute to increase the EPC constant but also produce a merge of two gaps widely distributed in the range of 41–75 meV at 20 K, leading to a higher T_c than fcc LaH_{10}. Therefore, we demonstrate that the multiband pairing of hybridized electronic states produces large anisotropic superconducting gaps in fcc LaH_{10} and YH_{10}.

We first present the electronic band structure of fcc LaH_{10}, obtained using the DFT calculations [31]. In all the calculations hereafter, we fix a pressure of 300 GPa favoring the fcc phase of LaH_{10} [21–23,26], where the optimized lattice parameters are $a = b = c = 4.748$ Å. As shown in Fig. 1(b), the calculated band structure exhibits four bands (denoted as $n = 1$, 2, 3, and 4) crossing E_F. The corresponding FS sheets are displayed in Fig. 1(c), together with the projection of their

*Corresponding author: chojh@hanyang.ac.kr

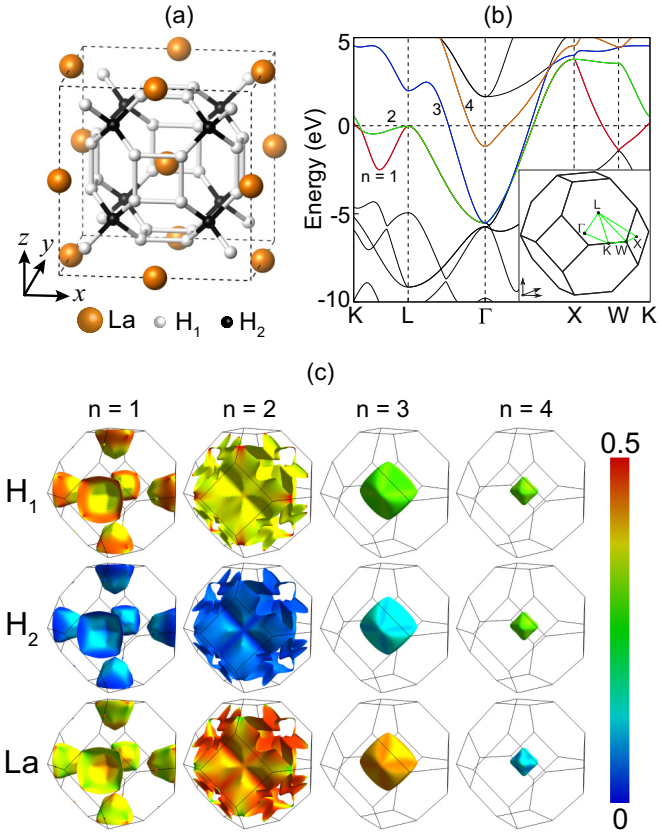

FIG. 1. (a) Optimized structure of the fcc phase of compressed LaH_{10}, composed of the cages of 32 H atoms surrounding a La atom. The two different types of H atoms, i.e., H_1 and H_2, are drawn with bright and dark circles, respectively. The positive x, y, and z axes point along the [001], [010], and [001] directions, respectively. (b) Calculated band structure of fcc LaH_{10} and (c) the corresponding FS sheets for the four bands of $n = 1$, 2, 3, and 4. The inset of (b) shows the Brillouin zone of the fcc primitive cell, where the Γ-X line is parallel to the x axis. In (c), the electronic state at each FS sheet is projected onto H_1, H_2, and La atoms using the color scale in the range [0, 0.5].

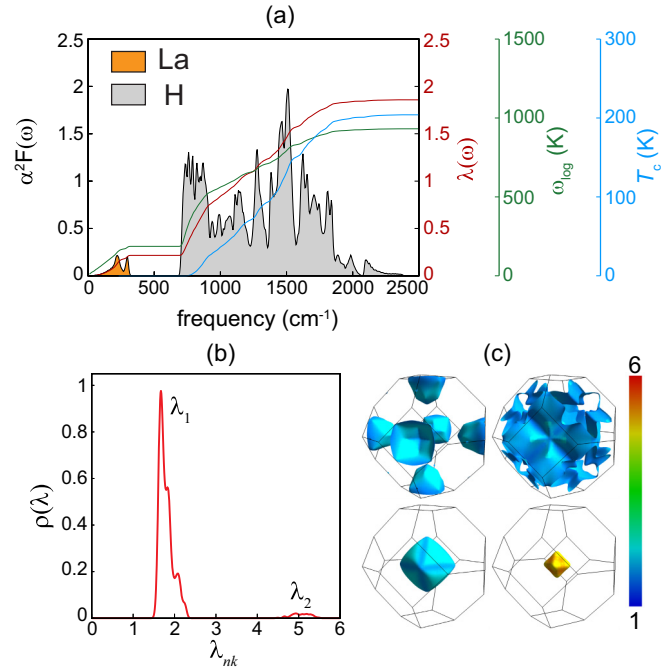

FIG. 2. (a) Isotropic Eliashberg function $\alpha^2F(\omega)$ (black), integrated EPC constant $\lambda(\omega)$ (red), $\omega_{\log}$ (green), and T_c (blue) of fcc LaH_{10}. (b) Distribution of $\mathbf{k}$-resolved EPC constant $\lambda_{n\mathbf{k}}$ and (c) the projected $\lambda_{n\mathbf{k}}$ on each FS sheet. In (b), the two separated regimes of $\lambda_{n\mathbf{k}}$ are indicated as λ_1 and λ_2.

electronic states onto the constituent atoms H_1, H_2, and La. The first FS sheet with the polyhedron shape around the X point is mostly composed of a hybridized state of H_1 s and La f orbitals (see Fig. S1 in the Supplemental Material [32]). The second FS sheet with the complex shape spreading over the large outer regions of the Brillouin zone is also composed of a hybridized state of H_1 s and La f orbitals (see Fig. S1 in the Supplemental Material [32]). The third and fourth FS sheets are topologically quite similar with concentric polyhedron shapes around the Γ point. However, these FS sheets have different orbital characters: i.e., the third one arises largely from a hybridized state of H_1 s and La f orbitals, whereas the fourth one is mainly due to a hybridized state of H_1 s or p and H_2 s orbitals (see Fig. S1 in the Supplemental Material [32]). It is noticeable that such hybridized electronic states near E_F could effectively screen the lattice vibrations involving H atoms, thereby giving rise to a strong EPC in fcc LaH_{10}. Further, the FS sheets with different orbital characters are expected to invoke different couplings between the various bands, leading to the emergence of anisotropic multiple SC gaps, as will be demonstrated later.

To illustrate an overview of the EPC and T_c of fcc LaH_{10}, we calculate the Eliashberg function $\alpha^2F(\omega)$ and integrated EPC constant $\lambda(\omega)$ using the isotropic Migdal-Eliashberg equations [28–30]. The calculated results together with the logarithmically average phonon frequency $\omega_{\log}$ are displayed in Fig. 2(a). We find that $\lambda(\omega)$ increases monotonously as ω increases up to the optical phonon modes with a high frequency of ∼1800 cm^{-1}, indicating that the lattice vibrational modes in the whole frequency range participate in the increase of $\lambda(\omega)$. It is noted that the four FS sheets distributed over the whole Brillouin zone provide the EPC channels with many phonon modes of widely distributed $\mathbf{q}$ wave vectors. Using the McMillan-Allen-Dynes formula [33], we estimate T_c as a function of ω [see Fig. 2(a)]. Although the McMillan-Allen-Dynes formula cannot properly describe anisotropic multiband SC, its estimation of $T_c(\omega)$ may give a qualitative aspect of how largely certain-frequency phonon modes contribute to T_c. As shown in Fig. 2(a), H-derived optical phonon modes contribute to a nearly linear increase of T_c with increasing ω. It is, however, interesting to note that, even though the acoustic phonon modes of La atoms provide ∼12% of the total EPC constant $\lambda = \lambda(\infty)$ [23,26], they hardly contribute to an increase of T_c [see Fig. 2(a)].

In order to examine the anisotropy in the EPC of fcc LaH_{10}, we use the anisotropic Migdal-Eliashberg equations [28–30] to calculate the $\mathbf{k}$-resolved EPC constant $\lambda_{n\mathbf{k}}$ for the electronic state $(n, \mathbf{k})$, which includes all available electron-phonon scattering processes connecting $\mathbf{k}$ and other $\mathbf{k}$ points on the FS sheets. The distribution of $\lambda_{n\mathbf{k}}$ and their projection on each

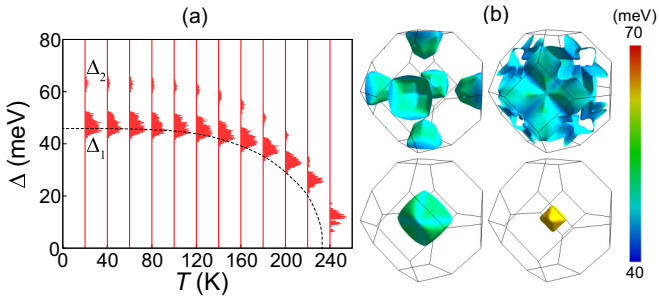

FIG. 3. (a) Energy distribution of the anisotropic superconducting gap Δ of fcc LaH_{10}. The two separated gaps are indicated as Δ_1 and Δ_2. The dashed line in (a) represents the Δ values, estimated using the isotropic Migdal-Eliashberg equations. (b) **k**-resolved superconducting gap $\Delta_{n\mathbf{k}}$ on the four FS sheets, computed at 20 K.

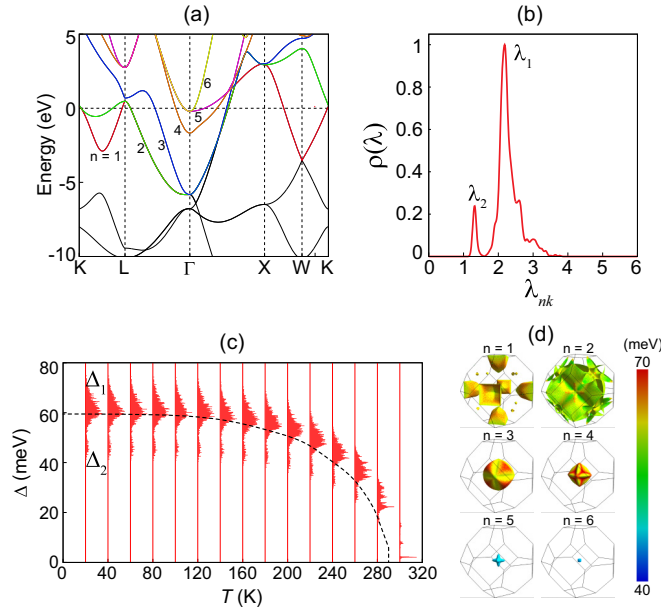

FIG. 4. (a) Calculated band structure of fcc YH_{10} at 300 GPa and (b) the distribution of $\lambda_{n\mathbf{k}}$. In (b), the two regimes of $\lambda_{n\mathbf{k}}$ are indicated as λ_1 and λ_2. (c) Energy distribution of Δ as a function of temperature and (d) $\Delta_{n\mathbf{k}}$ on the six FS sheets, computed at 20 K. The dashed line in (c) represents Δ estimated using the isotropic Migdal-Eliashberg equations.

FS sheet are plotted in Figs. 2(b) and 2(c), respectively. We find that there are two regimes of $\lambda_{n\mathbf{k}}$: i.e., the lower regime λ_1 in the range of 1.55–2.29 arising from the $n = (1, 2, 3)$ bands and the upper one λ_2 in the range of 4.49–5.49 arising from the $n = 4$ band. Here, it is noticeable that (i) the larger distribution of λ_1 is caused by the high density of states (DOS) of the hybridized $n = (1, 2, 3)$ states at E_F and (ii) the larger λ_2 values represent the strong EPC of the hybridized $n = 4$ state stemming from H_1 s or p and H_2 s orbitals. Thus, the division of the two regimes λ_1 and λ_2 indicates the different EPC strengths depending on the orbital characters of the hybridized electronic states on the FS sheets. We also note that some spreads of the λ_1 and λ_2 values feature the anisotropy of EPC, which is apparent from the projection of $\lambda_{n\mathbf{k}}$ on each FS sheet: i.e., the size of $\lambda_{n\mathbf{k}}$ changes with respect to the **k** directions on each FS sheet [see Fig. 2(c)].

It is natural that the two well-separated regimes of $\lambda_{n\mathbf{k}}$ in fcc LaH_{10} could give rise to two superconducting gaps. By numerically solving the anisotropic Migdal-Eliashberg equations [28–30] with a typical Coulomb pseudopotential parameter of $\mu^* = 0.13$ [21,22], we calculate the temperature dependence of superconducting gap Δ. Figure 3(a) displays the energy distribution of Δ as a function of temperature. We find that there are the two gaps Δ_1 and Δ_2, indicating a two-gap SC. These two gaps close at $T_c \approx 252$ K [see Fig. S2(a) in the Supplemental Material [32]]. For $T < 100$ K, Δ_1 (Δ_2) is distributed in the range of 41–52 (60–66) meV, and their separation is ~8 meV [see Figs. 3(a) and S3(a)]. Such sizable spread and separation of Δ_1 and Δ_2 are well compared with those [see Fig. S3(b)] of a typical high-T_c superconductor MgB_2 [34–39]. From the n- (see Fig. S4) and **k**-resolved [Fig. 3(b)] superconducting gap $\Delta_{n\mathbf{k}}$ on the FS, we reveal that the formations of Δ_1 and Δ_2 are associated with the $n = (1, 2, 3)$ and $n = 4$ bands, respectively. Thus, we can say that $\lambda_{n\mathbf{k}}$ and $\Delta_{n\mathbf{k}}$ are correlated with each other: i.e., the larger the magnitude of $\lambda_{n\mathbf{k}}$, the higher the $\Delta_{n\mathbf{k}}$ value. It is noticeable that the size of $\Delta_{n\mathbf{k}}$ changes on each FS sheet without any node, representing the anisotropic superconducting gaps with s-wave symmetry. In Fig. 3(a), the Δ values obtained from the isotropic Migdal-Eliashberg formalism are also plotted with the dashed line. Here, the gap closes around $T_c \approx 233$ K, smaller than that ($T_c \approx 252$ K) estimated from the anisotropic Migdal-Eliashberg formalism. Therefore, the anisotropy of electron-phonon interactions in multiple bands increases T_c only by ~10% (~19 K), similar to that (~10 K) of an anisotropic multigap superconductor, metallic hydrogen [40].

Based on our results of $\lambda_{n\mathbf{k}}$ and $\Delta_{n\mathbf{k}}$ in fcc LaH_{10}, we conclude that the predicted anisotropic EPC and superconducting gaps are attributed to the multiband pairing with the four FS sheets composed of the hybridized states of different orbital characters [see Fig. 1(c)]. To further demonstrate the importance of multiband pairing in high-T_c SC, we study the properties of $\lambda_{n\mathbf{k}}$ and $\Delta_{n\mathbf{k}}$ of fcc YH_{10} that was previously [20–22] predicted to exhibit higher T_c than fcc LaH_{10}. The geometry of fcc YH_{10} is the same sodalitelike clathrate structure as fcc LaH_{10} (see Fig. S5 in the Supplemental Material [32]). Figure 4(a) shows the calculated electronic band structure of fcc YH_{10} at 300 GPa. We find that fcc YH_{10} has very similar dispersions for the four bands of $n = 1$, 2, 3, and 4, as compared with those of fcc LaH_{10} [see Fig. 1(b)]. However, in fcc YH_{10}, the two electronlike bands of $n = 5$ and 6 originating mostly from Y d orbitals become occupied below E_F around the Γ point [see Figs. 4(a) and S6]. It is noted that the electron pockets of the $n = 5$ and 6 bands around the Γ point remain occupied in the local-density approximation (LDA) [41] and all-electron [42] calculations (see Fig. S7). Using the isotropic Migdal-Eliashberg formalism [28–30], we obtain $\lambda = 2.23$ and $T_c = 290$ K, larger than those ($\lambda = 1.86$ and $T_c = 233$ K) of fcc LaH_{10}. Figure 4(b) shows the calculated distribution of anisotropic $\lambda_{n\mathbf{k}}$ in fcc YH_{10}, where the peaks of the two regimes λ_1 and λ_2 locate at around 2.19 and 1.33, respectively. From the projection of $\lambda_{n\mathbf{k}}$ on each FS sheet, we find that λ_1 originates mostly from the $n = (1, 2, 3, 4)$ bands, while λ_2 is due to the $n = (5, 6)$ bands (see Fig. S8 in the Supplemental

Material [32]). Compared with the large $\lambda_{n\mathbf{k}}$ values (between 4.49–5.49) originating from the $n = 4$ band of fcc LaH_{10} [see Figs. 2(b) and 2(c)], the corresponding values of fcc YH_{10} are much reduced to about 2.20–3.79 [see Figs. S8 and S9(b)], which reflects the weakened intraband and interband coupling strengths of the $n = 4$ band as the $n = 5$ and 6 bands are occupied. However, the $\lambda_{n\mathbf{k}}$ values of the $n = (1, 2, 3)$ bands in fcc YH_{10} increase by ∼0.5, compared to the corresponding values in fcc LaH_{10}: see the n-resolved $\lambda_{n\mathbf{k}}$ of fcc LaH_{10} and YH_{10} in Fig. S9. Such an increase of EPC constant in fcc YH_{10} having the six FS sheets is likely due to more EPC channels than fcc LaH_{10} having the four FS sheets. We note that the $n = (5, 6)$ bands arising mostly from Y d orbitals with weak hybridization characters (see Fig. S6 in the Supplemental Material [32]) give rise to relatively smaller values of λ_2 [see Fig. 4(b)]. Figures 4(c) and 4(d) show the temperature dependence of Δ and the $\mathbf{k}$-resolved $\Delta_{n\mathbf{k}}$ on the six FS sheets, respectively. These results agree well with those obtained by a recent first-principles calculation of Heil *et al.* [20]. Contrasting with the well-separated two gaps in fcc LaH_{10}, the two gaps Δ_1 and Δ_2 in fcc YH_{10} are merged with each other, leading to a wide distribution of 41–75 meV for $T < 100$ K [see Fig. 4(c)]. From the n- (see Fig. S10) and $\mathbf{k}$-resolved [Fig. 4(d)] $\Delta_{n\mathbf{k}}$ on the FS, Δ_1 and Δ_2 are found to be associated with the $n = (1, 2, 3, 4)$ and $n = (5, 6)$ bands, respectively. These spreads of $\Delta_{n\mathbf{k}}$ with respect to the different bands and different $\mathbf{k}$ directions [see Fig. 4(d)] represent the anisotropy of superconducting gap in fcc YH_{10}. The resulting broad gap of fcc YH_{10} closes at $T_c \approx 308$ K [see Fig. S2(b) in the Supplemental Material [32]], higher than that [∼252 K in Fig. 3(a)] of fcc LaH_{10}.

Since the minima of the $n = (5, 6)$ bands of fcc YH_{10} are close to E_F, they are enabled to be unoccupied by the hole doping of $n_h > \sim 0.17e$ per unit cell (see Fig. S11 in the Supplemental Material [32]). In order to examine how the occupation of the $n = (5, 6)$ bands influences SC, we use the isotropic Migdal-Eliashberg formalism [28–30] to estimate the variations of λ and T_c with respect to the amount of n_h. We find that λ and T_c decrease monotonously with increasing n_h (see Table SI in the Supplemental Material [32]). As a result, T_c decreases from 290 K (without hole doping) to 269 K at $n_h = 0.3e$. It is thus manifested that the reduced number of FS sheets via hole doping decreases the EPC channels, resulting in a decrease of T_c. Interestingly, the hole doping in fcc LaH_{10} slightly increases T_c from 233 K (without hole doping) to 245 K at $n_h = 0.3e$ (see Table SI). We note that for $n_h = 0.3e$, despite the smaller EPC constant of YH_{10} compared to LaH_{10}, YH_{10} shows higher T_c than LaH_{10} (see Table SI). To explain this result, we plot the phonon dispersions of LaH_{10} and YH_{10} in Figs. S12(a) and S12(b), respectively. We find that YH_{10} has a logarithmically average phonon frequency of $\omega_{\log} = 1019$ cm^{-1}, which is much larger than that (748 cm^{-1}) for LaH_{10}. As shown in Fig. S12(c), the corresponding integrated $T_c(\omega)$ of YH_{10} is slightly lower than that of LaH_{10} up to $\omega \approx 2010$ cm^{-1}, while the former becomes higher than the latter above $\omega \approx 2010$ cm^{-1}. Thus, we can say that for $n_h = 0.3e$, the higher T_c in YH_{10} than in LaH_{10} would be associated with the increase in the frequencies of H-derived optical phonon modes.

In conclusion, our first-principles calculations for fcc LaH_{10} have shown that the hybridized states of La and H_1 atoms as well as H_1 and H_2 atoms on the four FS sheets are strongly coupled with the phonon modes in the whole frequency range, contrasting with a typical low-T_c BCS-type superconductor MgB_2 [43] where certain phonon modes significantly contribute to the EPC. Specifically, we reveled that the presence of such multiple FS sheets with different orbital characters gives rise to the two nodeless, anisotropic superconducting gaps on the FS. It is thus demonstrated that the two factors such as multiband pairing and the hybridized states of constituent atoms are characterized in the recently observed [1,2] room-temperature SC in fcc LaH_{10}. The present findings have important implications for understanding the detailed nature involved in high-T_c SC of compressed hydrides, as well as in tuning T_c through carrier doping.

This work was supported by the National Research Foundation of Korea (NRF) grant funded by the Korean Government (Grant No. 2019R1A2C1002975, No. 2016K1A4A3914691, and No. 2015M3D1A1070609). The calculations were performed by the KISTI Supercomputing Center through the Strategic Support Program (Program No. KSC-2019-CRE-0183) for the supercomputing application research.

[1] M. Somayazulu, M. Ahart, A. K. Mishra, Z. M. Geballe, M. Baldini, Y. Meng, V. V. Struzhkin, and R. J. Hemley, Phys. Rev. Lett. **122**, 027001 (2019).
[2] A. P. Drozdov, P. P. Kong, V. S. Minkov, S. P. Besedin, M. A. Kuzovnikov, S. Mozaffari, L. Balicas, F. F. Balakirev, D. E. Graf, V. B. Prakapenka, E. Greenberg, D. A. Knyazev, M. Tkacz, and M. I. Eremets, Nature (London) **569**, 528 (2019).
[3] A. P. Drozdov, M. I. Eremets, I. A. Troyan, V. Ksenofontov, and S. I. Shylin, Nature (London) **525**, 73 (2015).
[4] C. M. Pépin, G. Geneste, A. Dewaele, M. Mezouar, and P. Loubeyre, Science **357**, 382 (2017).
[5] X. Li, X. Huang, D. Duan, C. J. Pickard, D. Zhou, H. Xie, Q. Zhuang, Y. Huang, Q. Zhou, B. Liu, and T. Cui, Nat. Commun. **10**, 3461 (2019).
[6] I. A. Troyan, D. V. Semenok, A. G. Kvashnin, A. G. Ivanova, V. B. Prakapenka, E. Greenberg, A. G. Gavriliuk, I. S. Lyubutin, V. V. Struzhkin, and A. R. Oganov, arXiv:1908.01534.
[7] E. Zurek and T. Bi, J. Chem. Phys. **150**, 050901 (2019).
[8] J. A. Flores-Livas, L. Boeri, A. Sanna, G. Profeta, R. Arita, and M. Eremets, arXiv:1905.06693.
[9] J. Bardeen, L. N. Cooper, and J. R. Schrieffer, Phys. Rev. **106**, 162 (1957).
[10] N. W. Ashcroft, Phys. Rev. Lett. **21**, 1748 (1968).
[11] J. McMinis, R. C. Clay, D. Lee, and M. A. Morales, Phys. Rev. Lett. **114**, 105305 (2015).
[12] J. M. McMahon, M. A. Morales, C. Pierleoni, and D. M. Ceperley, Rev. Mod. Phys. **84**, 1607 (2012).
[13] R. P. Dias and I. F. Silvera, Science **355**, 715 (2017).

[14] W. A. Bassett, High Press. Res. **29**, 163 (2009).
[15] H. K. Mao, X. J. Chen, Y. Ding, B. Li, and L. Wang, Rev. Mod. Phys. **90**, 015007 (2018).
[16] H. Wang, J. S. Tse, K. Tanaka, T. Litaka, and Y. Ma, Proc. Natl. Acad. Sci. USA **109**, 6463 (2012).
[17] D. Duan, Y. Liu, F. Tian, D. Li, X. Huang, Z. Zhao, H. Yu, B. Liu, W. Tian, and T. Cui, Sci. Rep. **4**, 6968 (2014).
[18] X. Feng, J. Zhang, G. Gao, H. Liu, and H. Wang, RSC Adv. **5**, 59292 (2015).
[19] Y. Quan and W. E. Pickett, Phys. Rev. B **93**, 104526 (2016).
[20] C. Heil, S. di Cataldo, G. B. Bachelet, and L. Boeri, Phys. Rev. B **99**, 220502(R) (2019).
[21] F. Peng, Y. Sun, C. J. Pickard, R. J. Needs, Q. Wu, and Y. Ma, Phys. Rev. Lett. **119**, 107001 (2017).
[22] H. Liu, I. I. Naumov, R. Hoffmann, N. W. Ashcroft, and R. J. Hemley, Proc. Natl. Acad. Sci. USA **114**, 6990 (2017).
[23] L. Liu, C. Wang, S. Yi, K. W. Kim, J. Kim, and J.-H. Cho, Phys. Rev. B **99**, 140501(R) (2019).
[24] I. A. Kruglov, D. V. Semenok, R. Szczęániak, M. M. D. Esfahani, A. G. Kvashnin, and A. R. Oganov, Phys. Rev. B **101**, 024508 (2020).
[25] Y. Quan, S. S. Ghosh, and W. E. Pickett, Phys. Rev. B **100**, 184505 (2019).
[26] C. Wang, S. Yi, and J.-H. Cho, Phys. Rev. B **100**, 060502(R) (2019).
[27] P. Hohenberg and W. Kohn, Phys. Rev. **136**, B864 (1964); W. Kohn and L. J. Sham, *ibid.* **140**, A1133 (1965).
[28] A. B. Migdal, Sov. Phys. JETP **34**, 996 (1958).
[29] G. M. Eliashberg, Sov. Phys. JETP **11**, 696 (1960).
[30] P. B. Allen and B. Mitrović, Solid State Phys. **37**, 1 (1982).
[31] Our DFT calculations were performed using the Vienna *ab initio* simulation package (VASP) with the projector-augmented wave (PAW) method [44–46]. For the exchange-correlation energy, we employed the generalized-gradient approximation functional of Perdew-Burke-Ernzerhof (PBE) [47]. A plane-wave basis was taken with a kinetic energy cutoff of 500 eV, and the **k**-space integration was done with 24×24×24 k points for the structure optimization. All atoms were allowed to relax along the calculated forces until all the residual force components were less than 0.001 eV/Å. It is noted that the main peaks of La $4f$ orbitals in fcc LaH_{10} are located around ∼6 eV above E_F (see Fig. S14). Therefore, the present DFT study does not have any problem due to the localized nature of La $4f$ orbitals. The lattice dynamics and EPC calculations were carried out by using the QUANTUM ESPRESSO (QE) package [48] with the optimized norm-conserved Vanderbilt pseudopotentials (ONCV) [49] (see Fig. S15 in the Supplemental Material [32]) and a plane-wave cutoff of 1224 eV. Here, we used the 6×6×6 q points and 24×24×24 k points for the computation of phonon frequencies. For the calculation of EPC, we used the software EPW [39,50,51] with the 24×24×24 q points and 72×72×72 k points.
[32] See Supplemental Material at http://link.aps.org/supplemental/10.1103/PhysRevB.101.104506 for the band projections onto the orbitals of La, H_1, and H_2 atoms in fcc LaH_{10} and fcc YH_{10}. The estimation of T_c using the anisotropic Migdal-Eliashberg equations, the band structure of fcc YH_{10} with hole doping, and the band structures of fcc LaH_{10} and fcc YH_{10} obtained using PAW+PBE pseudopotentials in VASP and ONCV+PBE pseudopotentials in QE are also given.
[33] P. B. Allen and R. C. Dynes, Phys. Rev. B **12**, 905 (1975).
[34] F. Bouquet, R. A. Fisher, N. E. Phillips, D. G. Hinks, and J. D. Jorgensen, Phys. Rev. Lett. **87**, 047001 (2001).
[35] F. Giubileo, D. Roditchev, W. Sacks, R. Lamy, D. X. Thanh, J. Klein, S. Miraglia, D. Fruchart, J. Marcus, and Ph. Monod, Phys. Rev. Lett. **87**, 177008 (2001).
[36] M. Iavarone, G. Karapetrov, A. E. Koshelev, W. K. Kwok, G. W. Crabtree, D. G. Hinks, W. N. Kang, E.-M. Choi, H. J. Kim, H.-J. Kim, and S. I. Lee, Phys. Rev. Lett. **89**, 187002 (2002).
[37] S. Souma, Y. Machida, T. Sato, T. Takahashi, H. Matsui, S.-C. Wang, H. Ding, A. Kaminski, J. C. Campuzano, S. Sasaki, and K. Kadowaki, Nature (London) **423**, 65 (2003).
[38] K. Chen, W. Dai, C. G. Zhuang, Q. Li, S. Carabello, J. G. Lambert, J. T. Mlack, R. C. Ramos, and X. X. Xi, Nat. Commun. **3**, 619 (2012).
[39] E. R. Margine and F. Giustino, Phys. Rev. B **87**, 024505 (2013).
[40] P. Cudazzo, G. Profeta, A. Sanna, A. Floris, A. Continenza, S. Massidda, and E. K. U. Gross, Phys. Rev. B **81**, 134506 (2010).
[41] D. M. Ceperley and B. J. Alder, Phys. Rev. Lett. **45**, 566 (1980).
[42] V. Blum, R. Gehrke, F. Hanke, P. Havu, V. Havu, X. Ren, K. Reuter, and M. Scheffler, Comput. Phys. Commun. **180**, 2175 (2009).
[43] Y. Kong, O. V. Dolgov, O. Jepsen, and O. K. Andersen, Phys. Rev. B **64**, 020501(R) (2001).
[44] G. Kresse and J. Hafner, Phys. Rev. B **48**, 13115 (1993).
[45] G. Kresse and J. Furthmüller, Comput. Mater. Sci. **6**, 15 (1996).
[46] P. E. Blöchl, Phys. Rev. B **50**, 17953 (1994).
[47] J. P. Perdew, K. Burke, and M. Ernzerhof, Phys. Rev. Lett. **77**, 3865 (1996); **78**, 1396 (1997).
[48] P. Giannozzi, S. Baroni, N. Bonini, M. Calandra, R. Car, C. Cavazzoni, D. Ceresoli, G. L. Chiarotti, M. Cococcioni, I. Dabo *et al.*, J. Phys.: Condens. Matter **21**, 395502 (2009).
[49] M. J. van Setten, M. Giantomassi, E. Bousquet, M. J. Verstraete, D. R. Hamann, X. Gonze, and G. M. Rignanese, Comput. Phys. Commun. **226**, 39 (2018).
[50] F. Giustino, M. L. Cohen, and S. G. Louie, Phys. Rev. B **76**, 165108(R) (2007).
[51] S. Poncé, E. R. Margine, C. Verdi, and F. Giustino, Comput. Phys. Commun. **209**, 116 (2016).